Effects of Fe atoms on hardening of a nickel matrix: Nanoindentation experiments and atom-scale numerical modeling

L. Kurpaska [a,*], F.J. Dominguez-Gutierrez [a,d,*], Y. Zhang [b,c], K. Mulewska [a], H. Bei [e], W.J. Weber [b,c], A. Kosińska [a], W. Chrominski [a,f], I. Jozwik [a,g], R. Alvarez-Donado [a], S. Papanikolaou [a], J. Jagielski [a,g], M. Alava [a,h]

[a] NOMATEN Centre of Excellence, National Centre for Nuclear Research, st. A. Soltana 7, 05-400 Otwock, Poland
[b] Materials Science and Technology Division, Oak Ridge National Laboratory, Oak Ridge, TN 37831, USA
[c] Department of Materials Science & Engineering, University of Tennessee, Knoxville, TN 37996, USA
[d] Institute for Advanced Computational Science, Stony Brook University, Stony Brook, NY 11749, USA
[e] School of Materials Science and Engineering, Zhejiang University, Hangzhou 310027, China
[f] Faculty of Materials Science and Engineering, Warsaw University of Technology, st. Wołoska 141, 02-507 Warsaw, Poland
[g] Łukasiewicz Research Network – Institute of Microelectronic and Photonics, Wólczyńska 133 St., 01-919 Warsaw, Poland
[h] Department of Applied Physics, Aalto University, P.O. Box 11000, 00076 Aalto, Espoo, Finland

HIGHLIGHTS

- Hardening of Ni-based alloys has been studied by using experimental and numerical approach.
- Significant hardening as a function of Fe concentration has been observed.
- The main strengthening factors are associated to sluggish dislocation diffusion, reduced defect size and the nucleation of tetrahedral stacking faults.
- Interstitial type prismatic dislocation loops are formed during loading and their interaction leads to the formation of pyramidal shaped stacking faults.
- Both types of defects coexist in the same plastic deformation zone.

GRAPHICAL ABSTRACT
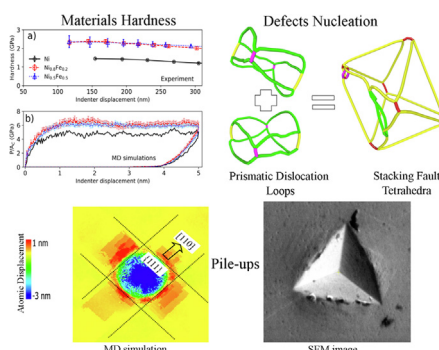
ARTICLE INFO

ABSTRACT

Significant hardening effect due to Fe concentrations in Ni-based alloys with face-centered-cubic structure has been studied by using a combined experimental and atomistic-based computational approach via nanoindentation tests. The obtained experimental load–displacement data for the [001] crystal orientation reached a qualitative good agreement with molecular dynamics simulations results, leading to strong evidence that the main strengthening factors are associated to sluggish dislocation diffusion, reduced defect sizes and the nucleation of tetrahedral stacking faults. Here, interstitial type prismatic dislocation loops mainly formed by $\frac{1}{6}\langle 112 \rangle$ Shockley dislocations are nucleated during the loading process, where their interaction leads to the formation of pyramidal shaped stacking fault which are mainly created by $\frac{1}{3}\langle 100 \rangle$ Hirth dislocations lines. Observing both types of defects coexisting in the same plastic deformation zone by both approaches. Reported mechanical data, measured experimentally and interpreted numerically, are also in accordance with microstructural SEM and TEM investigations.

* Corresponding authors.
  E-mail addresses: Lukasz.Kurpaska@ncbj.gov.pl (L. Kurpaska), Javier.Dominguez@ncbj.gov.pl (F.J. Dominguez-Gutierrez).

1. Introduction

Single phase concentrated solid solution alloys (SP-CSAs) are novel materials allowing to emphasize or delineate alloying effects [1,2]. In contrast to traditional alloy systems, SP-CSAs are composed of up to five principal elements that form concentrated random solid solutions in the simple underlying FCC or BCC lattice geometries [1–7]. The fundamental idea which drives research related to SP-CSA assumes that these materials show tunable levels of lattice distortion and chemical complexity [1,4] which results in reduction of the mean free path of electrons, phonons and magnons. Reported phenomena result in the modification of defect formation energies and migration barriers in SP-SCA alloys, and thus, SP-CSA systems appear as a new family of materials in which their desirable properties including defect stability, defect recombination and defect migration mechanisms that have to be experimentally tested and numerically simulated to be fully understood and explained. In this work, we investigate the detailed mechanisms in SP-CSAs with solely two elements (Ni, Fe) at variable relative concentration, using nanoindentation experiments and also, molecular simulations.

High-entropy alloys (HEAs) are multicomponent (four/five-element) versions of complex SP-CSAs, and they are considered to be strong candidates for structural components of future nuclear systems (i.e., Generation IV reactors, tokamaks, accelerators or fusion reactors), especially in cases where high radiation tolerance is a primary concern [8,9]. The origin of the behavior is believed to be strongly associated to the random nature of alloying elements in SP-CSAs, which may trigger recovery damage by efficient dynamic annealing at an early stage of the energy deposition [1,4,10]. In addition to very favorable radiation resistance, SP-CSAs show promising mechanical properties, such as high yield strength, high thermal stability and hardness, high-temperature strength, good wear and fatigue resistance, and excellent corrosion resistance in aggressive coolant media [11–13]. Reported properties were confirmed by both theoretical and experimental studies [4,14–16], however their responsible mechanisms are still prone to debate. For example, Jin et al. found that equiatomic NiFe presented significant delay in damage accumulation and evolution compared to pure nickel and NiCo at room temperature [17]. At the same time Lu et al. [13] have demonstrated that defect clusters migrate slower in NiFe than in pure nickel and NiCo at room temperature. This has been also confirmed by Molecular Dynamic (MD) simulations [18]. It is expected that similar responses will take place at elevated temperatures, however, underlying mechanisms are not clear and literature data about these processes is scarce.

In spite of these efforts, further study is required to examine the interplay between the dislocation loops evolution and local chemical segregation, particularly as a function of the chemical composition of SP-CSAs, with comparisons between experimental and numerical modelling data. Here, chemical complexity plays an important role due its connection with Stacking fault formation in SP-CSAs affecting the plastic deformation mechanism of $Ni_xFe_{(1-x)}$ materials. In general, available literature comparing experimental and atomistic simulations is scarce and there is a need for detailed studies of properties of the SP-CSA systems. Inspired by the previous discussion reported in literature, in this work, we conducted detailed nanomechanical investigations of three samples: pure nickel, $Ni_{0.8}Fe_{0.2}$ and $Ni_{0.5}Fe_{0.5}$ by using nanoindentation test [19–21]. The obtained experimental data for load–displacement (LD) curves and material hardness were compared with MD simulations, showing promising qualitative agreement. By using MD simulations [22], we investigated the mechanisms by which dislocations lines and dislocation loops mediate plastic deformation at early stages of nanoindentation in SP-CSAs. In conjunction with

available TEM data, we suggest that, for the studied SP-CSAs, the hardness increase in the material is driven by pyramidal shaped stacking faults that are formed by the interaction of interstitial-type prismatic dislocation loops formed principally by $\frac{1}{6}\langle 112\rangle$ dislocation lines. In addition, the observed prismatic loop sizes in simulations have a compositional dependence that is in line with TEM measurements. Thus, we believe that the combination of experimental and numerical efforts aids in understanding the deformation mechanism of SP-SCA systems.

Our manuscript is organized as follows: In Section 2, we describe the experimental techniques and computational methodology for carrying out nanoindentation tests. In Section 3, the hardness measurements and atomistic insights of indentation processes in crystalline pure nickel, $Ni_{0.8}Fe_{0.2}$ and $Ni_{0.5}Fe_{0.5}$ samples are presented, where an agreement between experimental measurements and numerical modelling is reported and discussed. Moreover, a discussion of dislocation nucleation mechanism provides information about the material hardness increase by including Fe in the alloy sample. In Section 4, we present a comparison of the experimental and simulation findings and discuss the implications of compositional complexity for defect properties. Finally, in Section 5, concluding remarks are summarized.

2. Experimental procedures and computational methods

To provide homogeneous and well mixed alloys, pure nickel and/or iron powders (>99.9% purity) were weighed and mixed by arc melting with the buttons flipped and re-melted five times ensuring good mixing before drop casting into a copper mold. Thus, single crystals were grown by using a floating-zone directional solidification method from the polycrystalline drop-cast ingots [23]. The diameter of the molten zone was carefully reduced in order to produce a neck that prevented slower growing grains from propagating [24,25]. The details of the single crystal growth are further detailed in Ref. [23]. Afterwards, X-ray backscatter Laue diffraction of pure Ni, $Ni_{0.8}Fe_{0.2}$ and $Ni_{0.5}Fe_{0.5}$ was performed, and results confirmed a single crystalline FCC structure for all tested specimens. Consecutively, all single crystals were re-oriented to [100] surface using backscatter Laue diffraction, and cut into disks with diameters of approx. 10 to 12.5 mm and thickness of 1.1 mm. The cutting procedure was performed by using an electro-discharge machine (EDM). Finally, all studied samples were carefully mechanically and electrochemically polished to remove the damaged layer created during cutting and mechanical polishing procedures.

The nanoindentation technique was utilized to measure materials hardness as function of indentation depth [19,20]. Prior to all experiments, a Diamond Area Function (DAF) of the indenter tip was calculated for each indentation depth. Calibrations were performed using Fused Silica (FS) as a standard material with defined mechanical properties. Measurements were performed at room temperature by using the Nanotest Vantage machine manufactured by Micro Materials Ltd with a force sensitivity is 3nN and the depth sensitivity is 0.002 nm. A diamond Berkovich-shaped indenter (Synton-MDP) was used for all the measurements. Nanoindentation tests were carried out in Load Partial Unload (LPU) mode [26,27]. This procedure was used to obtain a hardness response for different sized indents in the same spot. In this type of experiment, the force is increased to the maximum global force in a series of force-increasing and partial force removal increments. In our experimental set-up, we increased force from 0.5 mN to a maximum 10 mN every 0.5 mN up to 4 mN, and then at 5, 7 and 10 mN. At each maximum local force, the load was held constant for 2 s and then reduced to 30% of the max. force before reloading to the next force increment. Described procedure results in the obser-

vation of periodic serrations in the L-D curve. They, however, are related to the experimental procedure. It is known that metallic materials deform plastically once the applied stress exceeds the yield strength but also tend to creep (continued plastic deformation at constant applied stresses above the yield point). Creep causes error in the indentation measurement as it distorts the gradient of the force removal curve. To minimize this effect, hold time with max force was limited to 2 s. The described experimental procedure resulted in recording indentation depths between approx. 70 to 450 nm, depending on the specimen type. Each measurement was repeated 16 times with 50 μm spacing between the indents according to the schematics presented in Fig. 1. All the indents were made by using a loading/unloading rate of 0.5 mN/sec. The dwell period for drift data correction was set to 60 secs. The described methodology was used to minimize the impact of the surface quality (single indentations, if placed near scratches, would have been heavily impacted by improper contact between the indenter tip and sample surface).

Electron transparent lamellas of irradiation zone cross sections were taken with application of a standard lift-out technique on SEM/FIB ThermoFisher Scientific Helios 5 UX system. Thinning was conducted with gradually decreasing beam acceleration in order to minimize the impact of Ga ions on dislocation structures. TEM observations were carried out with JEOL JEM 1200EX II microscope operated at 120 kV. Particular care was taken to set a particular imaging conditions to make presented images comparable in terms of defects visibility. Sample was firstly tilted to the nearest ⟨001⟩ type zone axis and then two-beam condition with g = [200] was set to enhance contrast from dislocations. Dislocation density was calculated with line intercept method as utilized in Ref. [28]. Density was expressed with following formula $q = n/lt$ where n is the number of intersections of dislocations with experimental lines, l is the length of line grid, t is sample thickness. The latter was measured with a convergent beam diffraction method.

2.1. Molecular dynamics simulations framework

The numerical modelling aims to provide information about atomistic mechanisms during plastic deformation of the material during nanoindentation tests, and especially how the SP-CSA compositional complexity influences dislocation properties and mechanisms. One should take into account, that the identification of deformation mechanisms directly from nanoindentation experi-

mental data is very difficult, due to the presence of a complex stress profile underneath the indenter tip that induces non-trivial size effects. Thus, Molecular Dynamics offers an invaluable tool to get a deeper insight into processes occurring during nanoindentation. For this purpose, MD simulations of nanoindentation of pure nickel, $Ni_{0.8}Fe_{0.2}$ and $Ni_{0.5}Fe_{0.5}$ samples were performed by the Large-scale Atomic/Molecular Massively Parallel Simulator (LAMMPS) [29] and interatomic potentials reported by Choi et al. [30] which are based on the second Nearest Neighbor Modified Embedded Atom Method (2NN-MEAM). We first defined the initial Ni sample (see Table 1) and applied a process of energy optimization and equilibration for 100 ps with a Langevin thermostat at 300 K and a time constant of 100 fs [31,32]. This is done until the system reaches a homogeneous sample temperature and pressure profile [31], at a density of 8.78 gr/cm³. A final step is performed by relaxing the prepared sample for 10 ps to dissipate artificial heat. For the $Ni_{0.8}Fe_{0.2}$ and $Ni_{0.5}Fe_{0.5}$ samples, Ni atoms are substituted by Fe atoms randomly in the original FCC Ni sample following a thermalization at T = 300 K for 2 ns. The system is further equilibrated through the use of Monte Carlo (MC) relaxation, using a canonical ensemble with a compositional constraint by performing atomic swaps, as implemented in LAMMPS [29]. Converged configurations were cooled to T = 0 K and relaxed, to erase any thermal uncertainties. Finally, prepared samples are equilibrated at T = 300 K for 2 ns. All these simulations for pure nickel, $Ni_{0.8}Fe_{0.2}$ and $Ni_{0.5}Fe_{0.5}$ samples were performed in the isobaric-isothermal ensemble by means of integrating the Nose-Hoover equations with damping parameters τ_T = 2 fs and τ_P = 5 ps for the thermostat and barostat, respectively, and keeping the external pressure at 0 GPa, which reaches a density of 8.48 gr/cm³ for $Ni_{0.8}Fe_{0.2}$ and 8.17 gr/cm³ for the $Ni_{0.5}Fe_{0.5}$ sample. Before performing nanoindentation simulations, prepared samples are defined into three sections in the z direction for setting up boundary conditions along their depth, d_z: 1) the lowest bottom layers are kept frozen ($\sim$0.02 × d_z) to assure stability of the atoms when nanoindentation is performed; 2) a thermostatic region ($\sim$0.08 × d_z) above the frozen one is set to dissipate the generated heat during nanoindentation; and 3) the rest of the layers are defined as the dynamical atoms section, where the interaction with the indenter tip modifies the surface structure of the samples. Finally, a 5 nm vacuum section is added at the top of the sample [32].

Under the spatial (few nanometers) and time (picoseconds) scales of the MD simulations, the initial processes of the plastic deformation and phase transformation of the materials can be studied at the atomic level by nanoindentation testing. Here, a Berkovich tip can be modeled by a spherical indenter tip in the numerical modelling due to negligible differences between phase transformation regions presented by both tips at early stages of the loading process [33,34]. In addition, the roundness of the Berkovich tip validates the use of a spherical indenter in the MD simulations, which is limited to only few nm depths. Furthermore, the 1–100 m/s indentation velocity range, usually considered in MD simulations, is smaller than the sound's speed in solids, making the numerical modelling capable to accurately capture the elastic Hertzian regime and provide information of early dislocation nucleation, similar to those obtained in experiments, along with a better understanding of the elastic–plastic deformation transi-
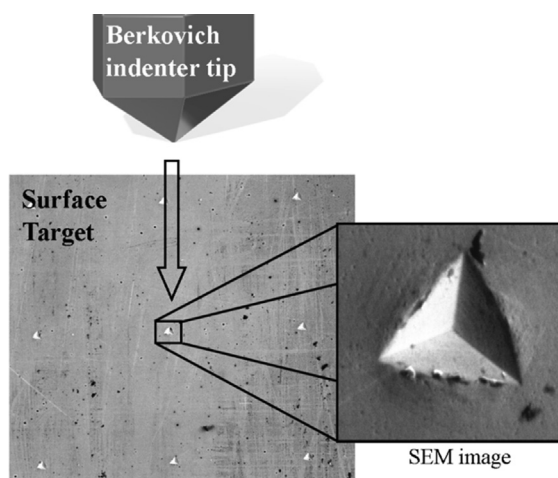

Fig. 1. Visualization of the mapping procedure during nanoindentation with Berkovich tip. A SEM image of the indenter tip mark is shown in the inset figure, where the surface topography of the $Ni_{0.5}Fe_{0.5}$ sample is presented after nanoindentation.

Table 1
Size and atomic distribution of the numerical samples used to perform MD simulations.

Sample	Size (dx,dy,dz) [nm]	Atoms
Nickel	(32.63, 35.47, 30.35)	3 164 800 Ni; 0 Fe
$Ni_{0.8}Fe_{0.2}$	(32.83, 35.68, 30.74)	2 531 840 Ni; 632 960 Fe
$Ni_{0.5}Fe_{0.5}$	(33.08, 35.95, 30.97)	1 582 400 Ni; 1 582 400 Fe

tion of the material. In our work, we use a NVE statistical thermo-dynamic ensemble to carry out the indentation test, where the velocity Verlet algorithm is implemented in LAMMPS with periodic boundary conditions set on the x and y axes to simulate an infinite surface [32]. A non-atomic repulsive imaginary (RI) rigid sphere defines our indenter tip as: $F(t) = K(r(t) - R)^2$ where the constant force is K = 37.8 MPa, and the trajectory of the center of the indenter tip is defined as $r(t) = (x_0, y_0, (z_0 \pm vt))$, with radius R = 5 nm, surface contact point as x_0 and y_0, and the initial gap $z_0 = 0.5$ nm between the surface and the intender tip to avoid effects of initial tip-surface interaction. The indenter tip's speed v = 50 m/s is chosen as positive for loading, and as negative for unloading processes. The LPU process was also emulated by the MD simulations where no qualitative difference was found to a monotonous loading process, which is further discussed in appendix A. Also, a comparison to a lower maximum tip's speed of 20 m/s is presented in the Supplementary Material (SM), where no qualitative differences with the obtained results were found. Each calculation was performed for 125 ps with a time step of $\Delta t = 0.5$ fs. for a maximum indentation depth of 5.0 nm to avoid the influence of boundary layers of the material. Thus, the load on the indenter P is computed by the forces acting on the indenter in the indentation direction and the depth h is calculated as the displacement of the indenter tip relative to the initial surface of the material sample.

3. Results

In order to estimate the mechanical properties changes recorded in pure Ni and two binary alloys with 20 and 50% Fe, all specimens were tested using the nanoindentation technique. In Fig. 2, we present the load–displacement (LD) dependencies obtained from different indentations and recorded for Ni in a) $Ni_{0.8}Fe_{0.2}$, in b) and $Ni_{0.5}Fe_{0.5}$ in c). The effect of the presence of Fe can be observed in Fig. 2b and Fig. 2c where the LD plots are more separated from each other. In other words: the increase of Fe content leads to an increase of the spread of results. This is particularly visible for $Ni_{0.5}Fe_{0.5}$ system (Fig. 2c) where the atomic percentage of Fe in the sample is higher. These results suggest that the substitution of Fe in the sample may not be uniform, or what is more likely, surface effects are more important in this specimen, as studied samples are single crystals, therefore, all elements should be distributed equally. For a given force, the indenter tip goes slightly deeper in the pure Ni sample, then for specimens with Fe addition. Moreover, relatively wider spreading of the load–displacement curves is observed with increasing Fe concentration, which may be associated with wider distributions of formation and migration energies of vacancies and interstitials with alloying Fe with Ni [1,2]. This result suggests that dislocation generation and propagation in pure Ni is easier than in binary alloys. This phenomenon has been confirmed by our simulations and further exploited in the following part of the paper.
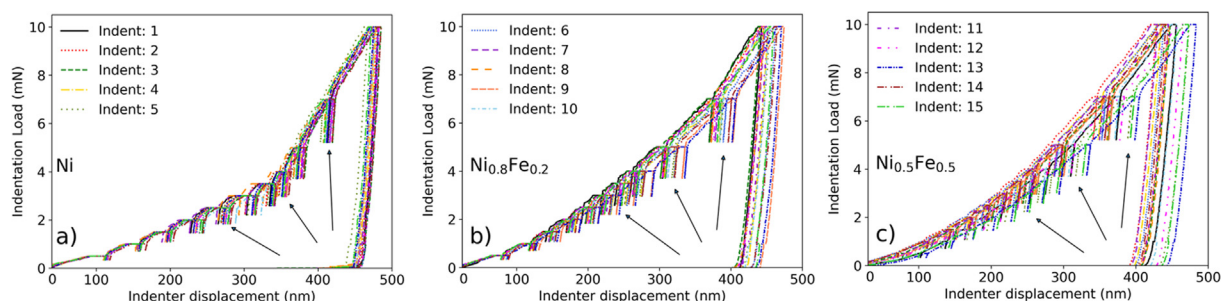
In Fig. 3, we present the representative LD plots from the experimental measurements in Fig. 3a and those obtained by the MD simulations in Fig. 3b for a single load-unload simulation. A comparison should be treated qualitatively and it is made in the elastic regime. For the MD results, 5 simulations were carried out at different locations on the $Ni_{0.8}Fe_{0.2}$ and $Ni_{0.5}Fe_{0.5}$ samples due to the random location of the Ni and Fe in the sample. An average of the LD curves, $P = 1/5\sum_{i=1}^{5}P_i$, from the MD simulations is presented in Fig. 3b with the error bars associated to the maximum and minimum values for all the simulations. For the Ni sample, one MD simulation was performed due to the symmetry of the single element sample. Although, MD allows us to simulate only 35000 nm^3 volume of the material, while recorded LD curves represent an almost 500 nm deep indentation; we note that indenter tip can penetrate the sample deeper for the Ni sample than for the $Ni_{0.8}Fe_{0.2}$ and $Ni_{0.5}Fe_{0.5}$ alloys for both cases. This result is related to the increase of material hardness in SP-CSAs. The elastic region in our MD simulations for the three samples is fitted to a Hertz fitting curve as:

$$P = \frac{4}{3}E_{Eff}R^{1/2}h^{3/2} \tag{1}$$

with R and h are the indenter tip radius and penetration depth, respectively; and E_{Eff} as the effectic elastic modulus of pure Ni or each binary alloys that considers the contributions of the sample and the indenter tip, and is defined as $\frac{1}{E_{Eff}} = \frac{1-v^2}{E^*} + \frac{1-v_i^2}{E_i}$ where (E^*, v) and (E_i, v_i) are the elastic modulus and Poisson radius of the sample and indenter tip, respectively. For the experimental part we consider a Poisson radius of 0.3 for the diamond tip and for the MD simulations this value is infinite due the spherical shaped IR tip. The sample material recovery is observed at the unloading curve where the maximum load is reached by the $Ni_{0.8}Fe_{0.2}$ sample with respect to the other two samples, besides the fast recovery of the studied binary alloys. This is also shown by the experimental data, where the $Ni_{0.8}Fe_{0.2}$ presented a higher hardness value than the other samples.

Fig. 4 compares hardness as a function of depth of three materials: pure Ni, $Ni_{0.8}Fe_{0.2}$ and $Ni_{0.8}Fe_{0.2}$ obtained experimentally and via MD. Fig. 4a shows recorded hardness values in the load range from 1 to 10 mN for all three studied samples. One can observe that in the case of pure nickel specimen, the hardness value oscillates around ~ 1.4 GPa in the whole indentation depth. It increases up to ~ 2.2 GPa for the specimen containing 20% Fe. When Fe content reaches 50%, the material hardness increases slightly further showing relatively large error bars. The reported trend qualitatively and quantitatively agrees with the work of Jin et al. [29] who tested similar sample compositions. Finally, one should mention that the presented H values agree with the tensile yield strength measurements [34]. Actually, a similar hardness value of pure Ni (1.18 ± 0.04 GPa) has also been recorded on [100] single crystals, by K. Jin et al. [35,36]. In the MD simulations, atomic resolution
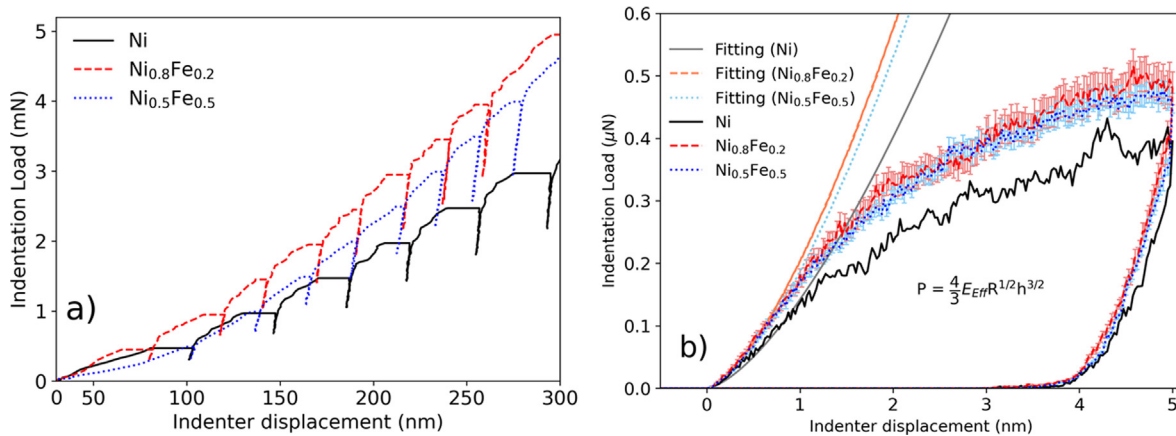

Fig. 2. Load- displacement dependencies for pure nickel, $Ni_{0.8}Fe_{0.2}$ and $Ni_{0.5}Fe_{0.5}$ alloys for several indents in the experiments. Arrows indicate serrations related to unloading process registered during LPU set-up.

Fig. 3. Load – displacement curve for pure nickel, $Ni_{0.8}Fe_{0.2}$ and $Ni_{0.5}Fe_{0.5}$ alloys obtained experimentally in a) and from MD simulations in b). Hertz fitting curves are included to the elastic region of our MD simulations and a qualitative good agreement is reached by both methods.
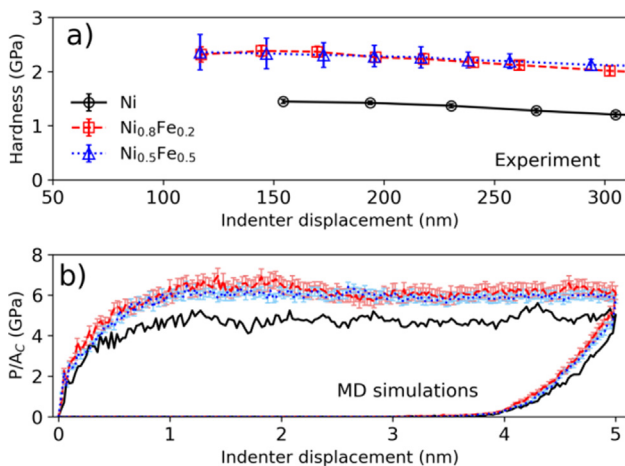

Fig. 4. Nanohardness of pure nickel, $Ni_{0.8}Fe_{0.2}$ and $Ni_{0.5}Fe_{0.5}$ as a function of the indenter displacement recorded during the nanoindentation test a) and loading and unloading parts for the MD simulations in b). Qualitative agreement in terms of hardness difference between individual samples and over penetration depth is reached by the theory and experimental measurements.

is achieved, so an inverse size effect at small depths is clearly visible, as it is well known to take place for spherical tips in FCC crystals [37]. Furthermore, standard size effects, such as the ISE proposed by the Nix-Gao model [38], are not clearly observed in either experiments or simulations, given the presence of submicrometer indentation depths, typically used to investigate ion-irradiated layers.

We note a trend in our MD simulations reported in Fig. 4b, where a qualitative agreement is reached to the experimental data. Here, the hardness is computed as H = P/Ac, with P as the load as a function of the indenter displacement and $Ac = \pi\left(2hR - h^2\right)$ as the contact area at load P, considering the indenter displacement, h, and tip radius, R. From MD simulation results, one can also notice that the hardness values do not show fluctuations as a function of the indenter tip penetration depth. They seem to stabilize after reaching a depth of 2.5 nm. We find that a combination of differences in the dislocation nucleation mechanisms, as well as the defect sizes, may explain the trend of hardness increase in the $Ni_{0.8}Fe_{0.2}$ and $Ni_{0.5}Fe_{0.5}$ samples with respect to pure Ni data. Starting by the realization that the trend presented by the experimental measurements for hardness is in a qualitative agreement to MD simulation results, we analyze dislocation nucleation mechanisms and defect sizes suggested by MD (described in what follows). We

show that our findings are consistent with Transmission Electron Microscopy (TEM) data, thus presenting a consistent picture of deformation mechanisms in SP-CSAs. In the SM, we present a qualitative good agreement between atomic displacement distributions that show the pile up formation after nanoindentation tests, in combination to those obtained by SEM images, for pure Nickel sample. Further, in the SM, we report the hardness values obtained by the Oliver Pharr method for several indentation depths, showing higher H values and a qualitative trend agreement with experimental data.

3.1. Dislocation nucleation mechanisms

In this section, we investigate the details of the dislocation density dynamics as a function of the indenter displacement, exploring differences among distinct chemical compositions. Obtained MD results are presented in Fig. 5 for pure Ni, in Fig. 6 for the $Ni_{0.8}Fe_{0.2}$ sample, and $Ni_{0.5}Fe_{0.5}$ is shown in Fig. 7. In order to investigate the mechanism of dislocation lines and loops nucleation, we apply the Dislocation Extraction Analysis (DXA) tool that is implemented in the software OVITO [39] to compute and visualize dislocation types dynamically. This provides an atomic insight into the plastic deformation of materials due to external loading. Thus, we compute the total dislocation density, ρ, as a function of the depth as.

$$\rho = \frac{l}{V_D} \tag{4}$$

where l is the dislocation length of each type, and $V_D = 2\pi/3(R_{pl}^3 - h^3)$ is the volume of the plastic deformation region by using the approximation of a spherical plastic zone; where R_{pl} is the largest distance of a dislocation measured from the indentation displacement, considering a hemispherical geometry. Here, the dislocation evolution as a function of the depth for different materials can be analyzed in Fig. 5a, Fig. 6a, and Fig. 7a).

In general, we note that the partial $\frac{1}{6}\langle112\rangle$ Shockley dislocations are dominant in all three samples, as expected for FCC crystals. From our MD simulations, it is also observed that the formation of the $\frac{1}{3}\langle100\rangle$ Hirth and $\frac{1}{6}\langle110\rangle$ Stair-rod partial dislocations start nucleating at a depth range of 0.5 to 1 nm for all specimens due to the stress profile underneath the indenter tip. These dislocations are responsible for prismatic dislocation loops (PDLs) nucleation that can be observed after reaching a penetration depth of 1.5 nm or deeper. Obtained numerical results suggest that the propagation of dislocation partials and loops is faster for pure Ni sample and starts to slow down as a function of increasing iron content in the studied samples, as reported in the SM through
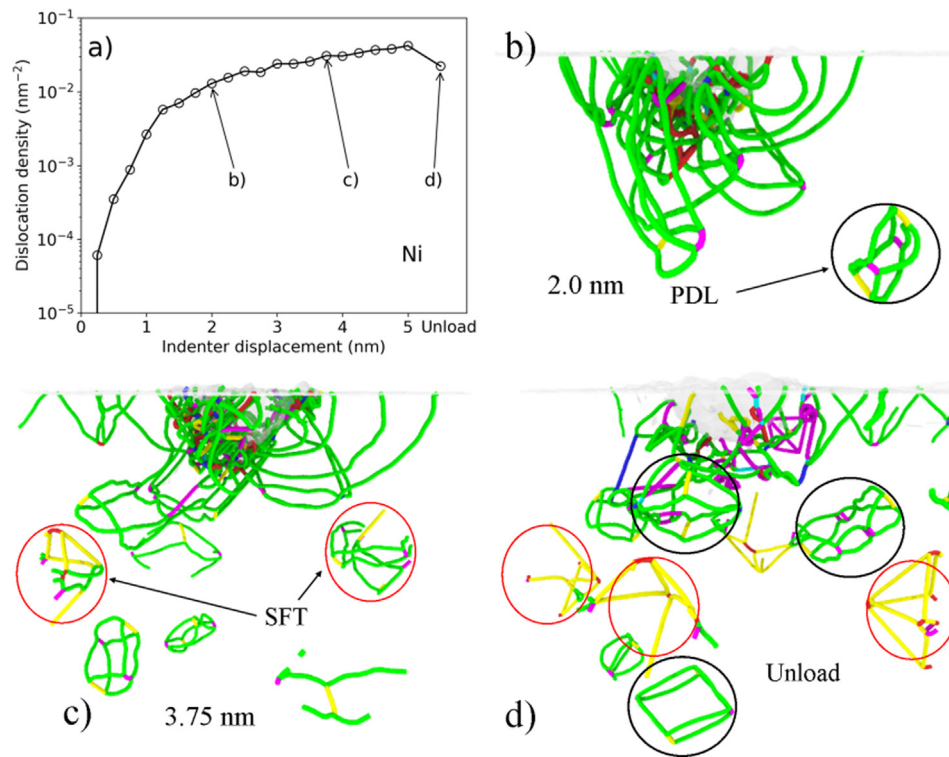
Fig. 5. Total dislocation density as a function of the indenter displacement for Ni in a), Prismatic dislocation loops (PDLs) and stacking fault tetrahedron (SFT) nucleation identification is shown in b)-d). PDLs and SFTs are identified by black and red circles, respectively. (For interpretation of the references to colour in this figure legend, the reader is referred to the web version of this article.)

Fig. 6. Total dislocation density as a function of the indenter displacement for $Ni_{0.8}Fe_{0.2}$ in a), PDLs and SFT nucleation mechanism in b-d). PDL and SFT are identified by black and red circles, respectively. (For interpretation of the references to colour in this figure legend, the reader is referred to the web version of this article.)
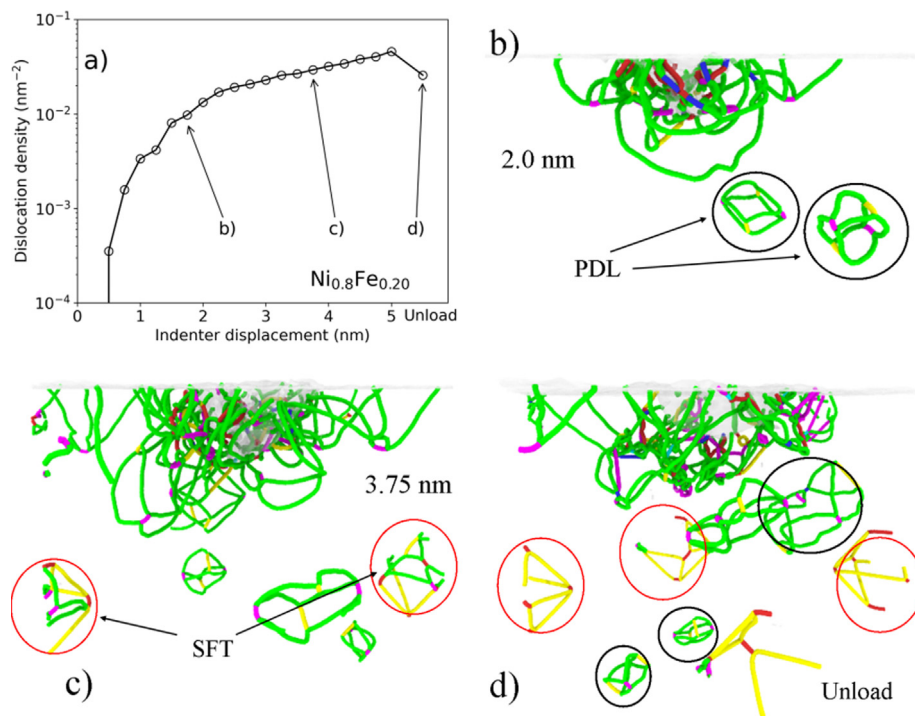
video animations of the MD simulations. Reported effects are in good agreement with TEM images where defects in pure Ni migrate faster than binary alloys [13]. In addition, the unloading process provides information about elastic recovery after the

nanoindentation cycle is terminated. Here, it is interesting to note that the $\frac{1}{6}\langle 112 \rangle$ Shockley dislocation partials decrease their lengths and some of them tend to disappear and being absorbed by the material surface.
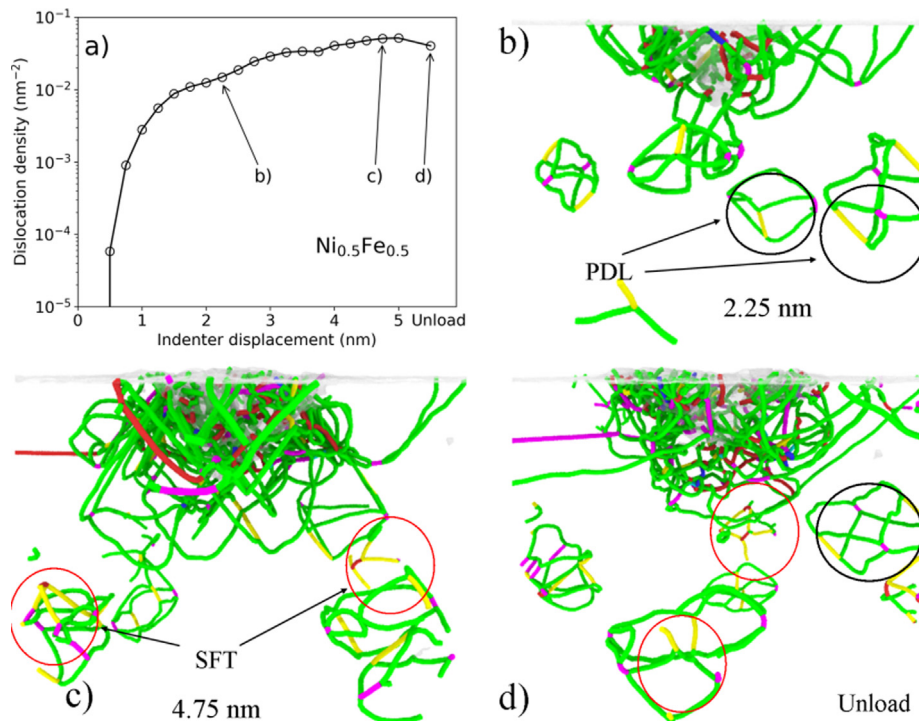
Fig. 7. Dislocation density for different dislocation types as a function of the indenter displacement for $Ni_{0.5}Fe_{0.5}$ in a), PDLs and SFT nucleation mechanism in b-f). PDL and SFT are identified by black and red circles, respectively. (For interpretation of the references to colour in this figure legend, the reader is referred to the web version of this article.)

For pure Ni, the formation of a PDL is observed at a depth of 2.0 nm which is a product of a lasso-type dislocation, as shown in a black circle in Fig. 5b. Then, at a depth of 2.50 nm, the nucleation of a second PDL, with a bigger radius than the first one is detected. A pyramidal shaped SFT is formed at a 3.75 nm depth (Fig. 5c), where the interaction of the PDLs occurs, identified by a red circle in Fig. 5d. SFTs are mainly formed by $\frac{1}{3}\langle 100 \rangle$ Hirth dislocation lines due the interaction of the PDL mainly formed by $\frac{1}{6}\langle 112 \rangle$ type Shockley dislocations. After 4.5 nm depth is reached, one can note the formation of two SFTs that remain in the plastic region after the unloading process occurs due to their slow mobility, see Fig. 5d. After the nanoindentation cycle is terminated, another type of SFT is formed by $\frac{1}{6}\langle 110 \rangle$ Stair-rod type dislocation lines which has also been observed in TEM images (for Ni samples). Finally, we conclude that pyramidally-shaped SFTs are formed by joining prismatic dislocation loops that are associated to the [100] crystal orientation of Ni.

The dislocation nucleation and evolution for the $Ni_{0.8}Fe_{0.2}$ sample is presented in Fig. 6. For the Ni sample an embryonic partial dislocation line was observed at 1 nm, but it was not formed for the Ni-Fe sample due to the Ni-Fe bonding. At 2 nm depth, two prismatic dislocation loops are already nucleated from the lasso dislocation in the {111} and {11−1} slip planes, as shown in Fig. 6b. Then, at a depth of 3.75 nm a SFT is already formed but few PDLs coexist in the plastic region (Fig. 6c). After 4.5 nm depth is reached, a couple of pyramidal shaped SFT are formed and followed the mechanism presented in the Ni sample. One should keep in mind that the described mechanism only concerns the [100] crystal orientation. After unloading, we note that both pyramidal SFT remained intact and do not move, Fig. 6d. In addition, the dislocation network that developed underneath the indenter, seems to be less dense compared to the one observed for the pure Ni sample. This phenomenon suggests that the $Ni_{0.8}Fe_{0.2}$ sample recovers faster than pure Ni, possibly contributing to the difference of reported experimentally material hardness.

In order to further investigate the mechanical response of binary alloys, we present the dislocation network dynamics of the

$Ni_{0.5}Fe_{0.5}$ system in Fig. 7. The presence of 50 % Fe in the sample appears to slow down the propagation of PDLs than in pure Ni sample, which is observed in the video animation of the MD simulation (see SM). It is noted that the 4th PDL is formed at depth of 3.75 nm for the $Ni_{0.5}Fe_{0.5}$ sample, while 5 PDLs are already formed for the other two cases. Here, the pyramidal SFT is not completely formed due to the slow propagation of PDLs, as observed in Fig. 7c. Clearly, it requires much deeper depth in order to achieve interaction between PDLs to finally form a pyramidal SFT. After unloading, the sample was able to recover with a couple of PDLs close to the dislocation network (underneath of the indenter tip), see Fig. 7d). The hardness of the material is similar as in the case of $Ni_{0.8}Fe_{0.2}$ due to the formation of a dislocation network density around the indenter that compensates for the absence of a second pyramidal SFT formed (as also observed for the $Ni_{0.8}Fe_{0.2}$ sample). In conclusion, our MD simulations show that vacancy-type SFT and interstitial-type PDL coexist in the same plastic region that is corroborated by the TEM images. The mechanism of the formation of tetrahedral stacking faults from prismatic dislocation loops is also observed in all studied samples. According to our studies, the mobility of PDLs seems to slow down with increasing Fe contribution, and the SFTs are not nucleated at a depth of 4 nm for the $Ni_{0.5}Fe_{0.5}$.

To better understand defect evolution in the studied pure Ni and binary alloys, we compared our results to TEM studies. Described samples were Ni-ion irradiated to a fluence of $5x10^{15}$ cm^{-2}, corresponding to a dose of approx. 6.5 dpa at the peak. Images are from about 500 nm depth, from the sample surface, therefore one can exclude surface related issues, like increased dislocation density originating into polishing processes. LPU nanoindentation test simulations were performed for a pure Ni sample, showing similar results for mechanical properties and dislocation network dynamics. These results are shown in the appendix section.

Fig. 8 shows that SFTs and dislocation loops (marked with red circles and blue arrows, respectively) coexist with each other, regardless of studied compositions. However, one can observe that

the size of dislocation loops decreases with increasing Fe content. Pure Ni specimen is characterized by large dislocations loops (as evidenced at Fig. 8A), but binary alloys (especially Ni$_{0.5}$Fe$_{0.5}$ sample), shows several small defects observed as black dots. According to Jin et al. [36], these defects were identified as small interstitial loops with few nm in size, or as a vacancy type stacking fault tetrahedron (SFT); which is in good qualitative agreement with the MD simulation results and also confirmed by the work of Lu et al. [13]. Information provided by TEM can be interpreted from a qualitative and quantitative point of view. One can see that the distribution of defect size for all three specimens, pure nickel, Ni$_{0.8}$Fe$_{0.2}$, Ni$_{0.5}$Fe$_{0.5}$ decreases. It seems that addition of Fe into the system, slows down the aggregation of the interstitial-type dislocation loops, as observed in MD simulations. One may interpret this result as increasing radiation resistance. In order to support our TEM observations, densities of large dislocations and small defects observable as black dots were calculated, see Table 2. One can see that in the case of small defects, density increases from 1.58×10^{22} 1/m^3 until 3.74×10^{22} 1/m^3, respectively for pure Ni and Ni$_{0.5}$Fe$_{0.5}$. Opposite situation takes place in the case of density of large dislocation loops, for pure Ni estimated value is about 2.93×10^{14} 1/m^2, while for Ni$_{0.5}$Fe$_{0.5}$ this parameter is not detectable as only small point defects are visible. Reported finding agrees with work of Lu et al [13] who reported similar trend.

According to the performed MD simulations, we categorized these dislocations into several dislocation types: ½⟨110⟩ (Perfect), 1/6 ⟨112⟩ (Shockley), 1/6 ⟨110⟩ (Stair-rod), 1/3 ⟨100⟩ (Hirth), 1/3 ⟨111⟩ (Frank). It is known that FCC materials form two types of dislocations: perfect dislocation loops of type a/2 ⟨110⟩ {110} and faulted dislocation loops of type a/3 ⟨ 111 ⟩ {111}, where a stands for lattice parameter. These dislocations are formed under neutron, ion or electron irradiation due to the irradiation pressure and cumulative defects by collision cascades. They can be also formed via standard metallurgical processes, e.g. quenching and are observed in many different materials like aluminum [40,41], steels [42], or nickel-based materials [43,44]. For this reason, we are able to compare structural data developed in FCC materials under mechanical loading (nanoindentation) and after irradiation. In general, it is known that perfect loops are mobile due to Burgers vectors that lie on the ⟨110⟩ direction, while faulted loops are sessile [44]. Therefore, pinned dislocation loops are considered as being responsible for hardening effects. According to our MD simulations, several types of loops emerge: 1/6 ⟨112⟩ (Shockley), 1/3 ⟨100⟩ (Hirth) and 1/3 ⟨111⟩ (Frank) loops. In the SM, we report the atomic distribution of shear strain and von Mises stress at the maximum indentation depth, directly from MD simulations. We observed that the increase of atomic percentages of Fe suppresses propagation of dislocation lines, and suppresses the size of PDLs and the plastic zone. Indeed, as shown in Fig. 9 and Table 2 (see also Section 4), the average PDL loop spanning area denoting the deformed region, decreases by approximately 20%, from ~ 75 nm^2 in pure Ni to ~ 50 nm^2 in equiatomic NiFe. (See Table 3).

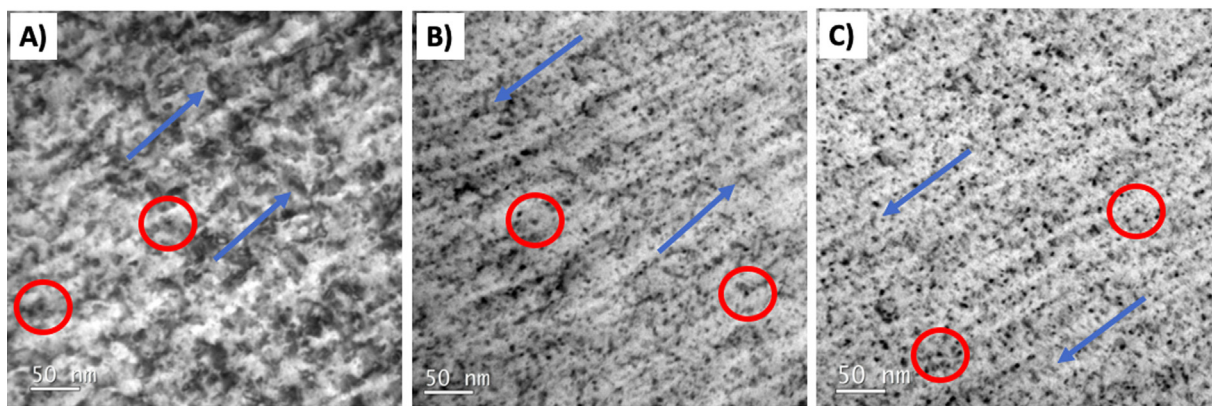**Fig. 8.** Images of the microstructure obtained by TEM: A) pure Ni, B) Ni$_{0.8}$Fe$_{0.2}$, and C) Ni$_{0.5}$Fe$_{0.5}$. Specimens were Ni-ion irradiated up to the fluence of 5×10^{15} cm^{-2}. One can observe typical SFT and dislocation loops which are marked with red circles and blue arrows, respectively. A decrease in the dislocation size is observed with increasing iron concentration in the system. (For interpretation of the references to colour in this figure legend, the reader is referred to the web version of this article.)
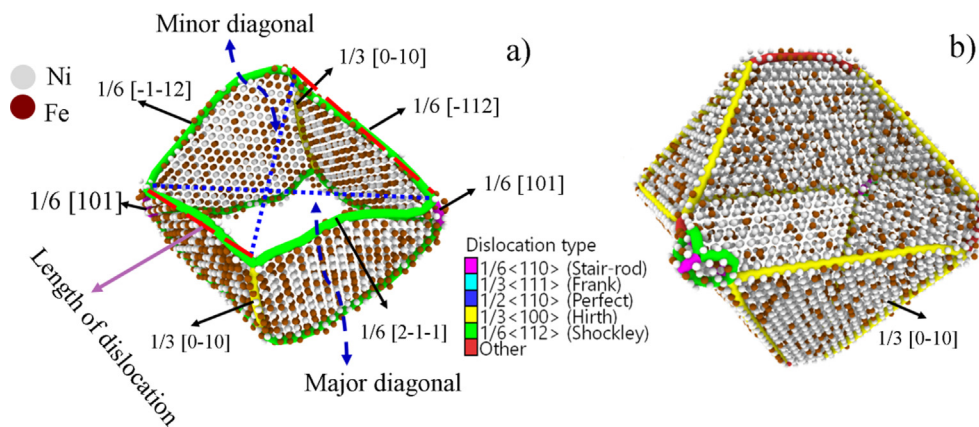

Fig. 9. Schematic of the characterization of the PDL in a) and SFT in b) for the Ni$_{0.5}$Fe$_{0.5}$ and Ni$_{0.8}$Fe$_{0.2}$ sample, respectively. We compute the area of the PDL by considering the length of the dislocation, as well as its minor and major diagonals. Noticing that the SFT nucleation is the result of the interaction of 2 PDL during the loading process due to the Shockley dislocation interactions that forms a Hirth type dislocation line. The *hcp* Ni and Fe atoms that create the stacking fault planar structure are depicted as gray and brown spheres, respectively.

Table 2

Dislocation and point defect density measured from samples imaged at Fig. 8 A – C).

Density of defects / Material	Pure Ni	Ni$_{0.8}$Fe$_{0.2}$	Ni$_{0.5}$Fe$_{0.5}$
Large defects (dislocation)	2.93×10^{14} 1/m^2	–	–
Small defects (point black dots)	1.58×10^{22} 1/m^3	1.93×10^{23} 1/m^3	3.74×10^{22} 1/m^3

4. Discussion

Table 3

Prismatic dislocation loops sizes for Ni, Ni$_{0.8}$Fe$_{0.2}$, and Ni$_{0.5}$Fe$_{0.5}$ by considering the characterization shown in Fig. 9. Total length of the PDL is computed as total Shockley + Stair-rod + Hirth lines and reported in units of [nm]. The area of the PDL is obtained as minor diagonal × major diagonal in units of nm^2.

Nickel				
PDL	Minor diagonal	Major diagonal	Area	Total length
1	5.05	5.13	25.91	33.98
2	7.60	7.82	59.51	47.20
3	6.88	7.80	53.71	45.07
4	8.91	10.0	89.11	57.93
5	8.25	9.37	77.39	51.80
Ni$_{0.8}$Fe$_{0.2}$				
1	4.34	4.90	21.31	31.13
2	4.34	4.90	21.31	28.71
3	6.76	7.24	48.94	44.89
4	8.12	8.36	67.92	50.24
Ni$_{0.5}$Fe$_{0.5}$				
1	6.27	7.04	44.15	44.27
2	5.47	5.73	31.40	37.53
3	7.34	7.66	56.28	50.37

Defect evolution during plastic deformation at room temperature in pure Ni, Ni$_{0.8}$Fe$_{0.2}$ and Ni$_{0.5}$Fe$_{0.5}$ systems were studied experimentally by using nanoindentation tests and interpreted by using MD simulations. In this work, we investigate dislocation generation mechanisms and the effect of increasing Fe presence in Ni-based samples. The implementation of the numerical modeling for nanoindentation tests is done in accordance to experimental conditions by tracking atomic strains and dislocation network dynamics. Although the volume and time scales of experimental tests and MD simulations are very different, it was possible to obtain a qualitative agreement between experimental and simulation data. The agreement has been confirmed by the trends observed for the materials' hardness as a function of the indentation depth, as well as for the typically obtained load–displacement curves in nanoindentation tests. From MD simulations, we observed the formation of pyramidal shaped stacking fault tetrahedron at the maximum indentation depth, that are nucleated by the interaction and join of PDLs developed along the [1 0 0] crystal orientation for pure Ni. It has been also shown that the presence of Fe in the Ni$_{0.2}$Fe$_{0.8}$ and Ni$_{0.5}$Fe$_{0.5}$ samples slows down the propagation of interstitial-type PDLs and the consequent stacking fault formation. We also observed a correlation between the number of formed dislocation loops and the percentage of Fe in the Ni system at the beginning of the plastic deformation process. Described in this work, dislocation network dynamics differences between pure Ni metal and Ni-Fe alloy systems can explain the difference of hardness for this kind of materials and be treated as a first step towards understanding plastic deformation mechanism and radiation resistance of SP-CSAs.

Point defects, their formation, migration, evolution, and the nucleation of different types of interstitial dislocation loops are the primary sources of microstructural changes that affect the mechanical properties of the materials. Therefore, controlling defect formation and migration is critical in designing materials with desired properties like resistance to radiation or high mechanical strength. Few studies have demonstrated the link between energy dissipation and defect evolution due to ferro and/or anti-ferromagnetic interactions exist [46]. These phenomena may be correlated with the delayed hardening effect, reported in single-phase concentrated solid solution alloys. Nickel and Iron have ferromagnetic properties below the Curie temperature [47]. At the same time, it is known that the addition of Fe in Ni delays defect evolution under irradiation at room temperature, especially in a high fluence regime [48], as shown in our MD simulations during the loading process. It has been proved that random site occupancy in SP-CSAs leads to a lack of translational symmetry. As a result, the electronic band structure is expected to smear out in reciprocal (k) space. Calculation of the electronic structure of pure Ni, NiCo, NiFe, NiFeCo, NiCoCr, and NiFeCoCr, which are 3d transition metals, has shown that the nickel has a well-defined electronic band structure. At the same time, the band structures of other studied alloys (also NiFe) are smeared out to very different extents in both energy and k-space [49]. This proves that the disordered electronic structure substantially reduces the electron mean free path, so the effectiveness of the energy dissipation of a complex system decreases. This is particularly important in the case of radiation damage build-up. It has been proved that above 1 dpa [50] ion damage range exceeds the theoretically predicted depths. This suggests alteration of the migration mobility in complex alloys. Besides, the disordered local structure of the SP-CSA plays a vital role in stacking fault formation during plastic deformation [51].

Moreover, recent TEM studies proved that defects migrate much faster in pure Fe than in NiFe or NiCo [5], as presented in our work. Pure nickel also shows a wider damage range than a binary system. This confirms higher defect mobility in pure Ni. In conclusion, migration of defects in a more complex system, the pure Ni (e.g., NiFe or NiCo), contributes to an enhanced defect recombination rate, which leads to a higher radiation tolerance. From the mechanical point of view, this is observable as a sluggish hardening effect, especially in a high fluence regime. In Fig. 9a) we present the characterization of PDL obtained at the maximum indentation depth for the Ni$_{0.5}$Fe$_{0.5}$ where their associated Burgers vectors are displayed. We also presented the parameters that are used to measure and identify this kind of material defects. This is particularly important when it comes to irradiation-induced defect evolution and related to its material hardening. In FCC structure, the loop growth is believed to have the biggest impact on degradation of the mechanical properties. This property change can be detected via hardening where induced dislocation loops act as obstacles for dislocation motion. In addition, hexagonal close-packed, *hcp*, Ni and Fe atoms that create the local stacking fault structure are depicted as gray and brown spheres, respectively. This shows the chemical complexity of the Ni$_x$Fe$_{(1-x)}$ materials affecting the formation of stacking faults due to atomic disorder of the samples [52– 58], especially for the equiatomic NiFe sample where defect dynamics is slower compared to pure Ni, as reported in the literature [53,54]. It is important to remark that the Ni$_x$Fe$_{(1-x)}$ samples are random solid solutions and there is a variation of the incipient short-range order (SRO) that depends on the annealing temperature; in molecular simulations, that would be the temperature at which Monte Carlo swaps are applied, T = 300 K and thus, creating spatial heterogeneities [55]. The SRO is expected to generate obstacles to the dislocation evolution and enhancing the strength of the sample where the equiatomic alloy is affected due to its high level of SRO [56].

In Fig. 9b), we present the formation of the pyramidal shaped SFT for the Ni$_{0.8}$Fe$_{0.2}$ sample that was observed at the maximum indentation depth and after nanoindentation test. It is clearly noted that this defect is mainly formed by Hirth dislocation and

hpc atoms for all the system. This process is typical for FCC materials where the {-1–11} ⟨110⟩ slip system present these kind of partial dislocations, in our case we obtain the process: 1/6[1–12] + 1/6[-1–1–2] → 1/3[0–10], for example. Besides, it is commonly assumed that deformation twinning is favored in low Stacking Fault Energy (SFE) materials like our $Ni_xFe_{(1-x)}$ species and dislocation slip dominates in high SFE materials [56], thus different SP-CSAs present a weak dependence on the number of elements, but present strong dependence on the charge redistribution in the stacking fault region [58], and thus SRO features, indicating the importance of both the types of alloying elements and their concentrations, as shown by our MD results; modifying the dislocation network of the plastic deformation region. Finally, the similarities between the process for stacking fault formation of pure Ni and $Ni_xFe_{(1-x)}$ is also observed during the loading process, where the SFE favors {-1–11} ⟨112⟩ shear deformation, leading to the nucleation of Shockley dislocations, as reported for irradiated CSAs and by our MD simulations at early stages of nanoindetantion test [57,58].

In this work we report in detail the evolution of dislocation loops during plastic deformation induced by nanoindentation of pure nickel, $Ni_{0.8}Fe_{0.2}$ and $Ni_{0.5}Fe_{0.5}$ specimens. In Table 3, we report the area and total dislocation length of stable PDL at the maximum indentation depth that are in full agreement with work of Jin et al. [35], where TEM studies suggested that increasing concentration of Fe increases defect concentration but reduces their size. In addition to that, the presence of SFTs and PDLs have been pointed out. Our work describes the evolution of dislocation loops, starting from early stages of their creation (partials) and finishing on fully stable stacking fault tetrahedrons, followed by prismatic dislocation loops evolution. It can be concluded that defects in Ni migrate faster than in binary systems and both vacancy type stacking fault tetrahedra and interstitial loops coexist in the same region. Slow migration of defects in SP-CSAs is also known as sluggish diffusion [1–4]. Moreover, our research indicates that SFTs are created as a result of interaction between PDLs.

Further, it is believed that addition of Fe delays large defect evolution and ultimately reduces volume swelling of the material, highlighting the importance to develop a deep understanding and characterization of dislocation loops in FCC systems, like the systematic work of Xiu et al. [45]. The final observed defect distributions in pure Ni, $Ni_{0.8}Fe_{0.2}$ and $Ni_{0.5}Fe_{0.5}$ systems are the integrated experimental and numerical results of defect production, recombination, migration and clustering. It is believed that chemical complexity leads to a distorted solid solution that can modify and tune energy dissipation and transport through electrons and phonons, subsequently impacting defect formation and evolution [1,4]. Some studies indicate that electron mean free paths may be reduced with increasing chemical complexity. The conducted MD results suggest that defect migration barriers are higher for SP-CSAs with higher chemical complexity than for pure nickel. Results of this study confirm the MD predictions that point defects and defect clusters migrate slower in both types of SP-CSAs than in pure nickel. It is therefore possible to speculate that defect recombination rate would increase because defect migration may occur only in localized areas in SP-CSAs, rather than in pure nickel. Therefore, these materials may have shown much higher radiation tolerance under harsh irradiation conditions.

5. Conclusions

In summary, a synergistic study, combining experimental and numerical data, has been conducted. We described defect range and evolution in single crystalline nickel and two Ni-based binary alloys, using nanoindentation tests and by an atomistic dislocation computational modelling. Obtained trend agreement in hardness data between experiments and simulations, led to atomistic simulations evidence that Fe concentration in SP-CSAs has a combined effect: Dislocation defects undergo sluggish diffusion at higher densities and infused PDLs are microstructurally smaller. SFTs are mainly formed by $\frac{1}{3}\langle 100 \rangle$ Hirth dislocation lines due to the interaction of interstitial type dislocation loops formed principally by $\frac{1}{6}\langle 112 \rangle$ dislocations lines during the loading process. In this way, the present study validates experimentally obtained TEM data which showed that dislocation loops lay on {111} slip plane, and the existence of extra planes confirms the presence of interstitial loops with Burgers vector b=$\frac{1}{3}\langle 111 \rangle$, which is adjacent to a small stacking fault tetrahedron.

Declaration of Competing Interest

The authors declare that they have no known competing financial interests or personal relationships that could have appeared to influence the work reported in this paper.

Appendix A:. Load - partial unload nanoindentation simulations

In order to investigate the effects of the load partial unload (LPU) nanoindentation tests on the mechanical properties of Ni-based alloys, we performed MD simulations by following the experimental setup and conditions, as close as possible. In Fig. 10a, we present results for the LD curves of the LPU nanoindentation test, comparing to monotonous-load nanoindentation results. The partial unloading was set at 1, 2, 3, and 4 nm depth for 0.1 nm unloading. The LD curves present a similar load at the maximum indentation depth, where the hardness of the material can be calculated by Oliver-Pharr method (see SM). In addition, the dislocation network formed at the maximum indentation depth is presented in Fig. 10b, and pyramidal shaped stacking fault tetrahedrons (SFT), as well as prismatic dislocation loop (PDLs) are observed. From the MD simulations, we noticed the same mechanism for formation and nucleation of SFTs and PDLs than that for the monotonous-load indentation simulations. In conclusion, for pure Ni samples, the LPU and single load nanoindentation simulations provide similar results and the latter is considered reasonable to qualitatively investigate the mechanical response of these material due to external loads.
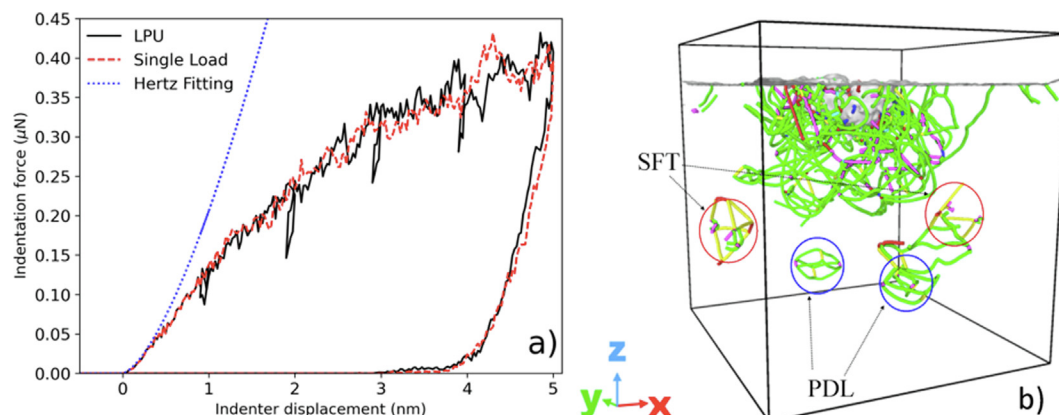
Fig. 10. LD curves for single load and load partial unload (LPU) nanoindentation tests for Nickel in a). Dislocation network at the maximum indentation depth in b) where stacking fault tetrahedron and prismatic dislocation loops are observed.

Appendix B. Supplementary data

Supplementary data to this article can be found online at https://doi.org/10.1016/j.matdes.2022.110639.

References

[1] Y. Zhang, Y.N. Osetsky, W.J. Weber, Tunable Chemical Disorder in Concentrated Alloys: Defect Physics and Radiation Performance, Chem. Rev. 122 (1) (2022) 789–829.

[2] Y.N. Osetskiy, L. Beland, A. Barashev, Y. Zhang, On the Existence and Origin of Sluggish Diffusion in Chemically Disordered Concentrated Alloys, Curr. Opin. Solid State Mater. Sci. 22 (2018) 65–74, https://doi.org/10.1016/j.cossms.2018.05.003.

[3] Y.N. Osetsky, A. Barashev, Y. Zhang, Sluggish, Chemical Bias and Percolation Phenomena in Atomic Transport by Vacancy and Interstitial Diffusion in Ni-Fe alloys, Curr. Opin. Solid State Mater. Sci. 25 (2021), https://doi.org/10.1016/j.cossms.2021.100961 100961.

[4] Y. Zhang, T. Egami, W.J. Weber, Dissipation of radiation energy in concentrated solid-solution alloys: Unique defect properties and microstructural evolution," vol. 44, pp. 798–811, (2019), doi: 10.1557/mrs.2019.233.

[5] B. Gludovatz, A. Hohenwarter, D. Catoor, E.H. Chang, E.P. George, R.O. Ritchie, A fracture-resistant high-entropy alloy for cryogenic applications, Science 345 (2014) 1153–1158, https://doi.org/10.1126/science.1254581.

[6] F. Otto, Y. Yang, H. Bei, E.P. George, Relative effects of enthalpy and entropy on the phase stability of equiatomic high-entropy alloys, Acta Mater. 61 (7) (2013) 2628–2638, https://doi.org/10.1016/j.actamat.2013.01.042.

[7] E. Resistivity, High-entropy Alloys with High Saturation, Magnetization, electrical Resistivity and Malleabilety, Sci. Rep. 3 (2013) 1–7, https://doi.org/10.1038/srep01455.

[8] E. J. Pickering, A. W. Carruthers, P. J. Barron, S. C. Middleburgh, D. E. J. Armstrong, and A. S. Gandy, High-Entropy Alloys for Advanced Nuclear Applications, Entropy, pp. 1–28, (2021), doi.org/10.3390/e23010098.

[9] T. Egami, W. Guo, P.D. Rack, T. Nagase, Irradiation resistance of multicomponent alloys, Metall. Mater. Trans. A 45 (1) (2014) 180–183, https://doi.org/10.1007/s11661-013-1994-2.

[10] Y. Zhang, G.M. Stocks, K. Jin, C. Lu, H. Bei, B.C. Sales, L. Wang, L.K. Beland, R.E. Stoller, G.D. Samolyuk, M. Caro, A. Caro, W.J. Weber, Influecne of chemical disorder on energy dissipation and defect evolution in concentrated solid solution alloys, Nat. Commun. (2015), https://doi.org/10.1038/ncomms9736.

[11] L.J. Santodonato, Y. Zhang, M. Feygenson, C.M. Parish, M.C. Gao, R.J.K. Weber, J. C. Neuefeind, Z. Tang, P.K. Liaw, Deviation from high-entropy configurations in the atomic distributions of a multi-principal-element alloy, Nat. Commun. 6 (1) (2015), https://doi.org/10.1038/ncomms6964.

[12] Z. Li, K.G. Pradeep, Y. Deng, Z. Li, D. Raabe, C.C. Tasan, Metastable high-entropy dual-phase alloys overcome the strength-ductility trade-off, Nature 534 (7606) (2016) 227–230, https://doi.org/10.1038/nature17981.

[13] C. Lu, K. Jin, L.K. Béland, F. Zhang, T. Yang, L. Qiao, Y. Zhang, H. Bei, H.M. Christen, R.E. Stoller, L. Wang, Direct observation of defect range and evolution in ion-irradiated single crystalline Ni and Ni Binary Alloys, Nat. Publ. Gr. no. February (2016) 1–10, https://doi.org/10.1038/srep19994.

[14] K. Jin, C. Lu, L.M. Wang, J. Qu, W.J. Weber, Y. Zhang, H. Bei, Effects of compositional complexity on the ion-irradiation induced swelling and hardening in Ni-containing equiatomic alloys, Scr. Mater. 119 (2016) 65–70, https://doi.org/10.1016/j.scriptamat.2016.03.030.

[15] F. Granberg, K. Nordlund, M.W. Ullah, K. Jin, C. Lu, H. Bei, L.M. Wang, F. Djurabekova, W.J. Weber, Y. Zhang, Mechanism of Radiation Damage Reduction in Equiatomic Multicomponent Single Phase Alloys, Phys. Rev.

Lett. vol. 116, no. 135504(April) (2016) 1–8, https://doi.org/10.1103/PhysRevLett.116.135504.

[16] N.A.P.K. Kumar, C. Li, K.J. Leonard, H. Bei, S.J. Zinkle, Microstructural stability and mechanical behavior of FeNiMnCr high entropy alloy under ion irradiation, Acta Mater. 113 (2016) 230–244, https://doi.org/10.1016/j.actamat.2016.05.007.

[17] K. Jin, H. Bei, Y. Zhang, Ion irradiation induced defect evolution in Ni and Ni-based FCC equiatomic binary alloys, J. Nucl. Mater. 471 (2016) 193–199, https://doi.org/10.1016/j.jnucmat.2015.09.009.

[18] D.S. Aidhy, C. Lu, K. Jin, H. Bei, Y. Zhang, L. Wang, W.J. Weber, Point defect evolution in Ni, NiFe and NiCr alloys from atomistic simulations and irradiation experiments, Acta Mater. 99 (2015) 69–76, https://doi.org/10.1016/j.actamat.2015.08.007.

[19] A.M. Minor, S.A.S. Asif, Z.W. Shan, E.A. Stach, E. Cyrankowski, T.J. Wyrobek, O.L. Warren, Nat. Mater. 5 (2006) 697.

[20] C.A. Schuh, Nanoindentation studies of materials, Mater. Today 9 (5) (2006) 32–40.

[21] J.K. Mason, A.C. Lund, C.A. Schuh, Determining the activation energy and volume for the onset of plasticity during nanoindentation, Phys. Rev. B 73 (2006) 054102.

[22] G.Z. Voyiadjis, M. Yaghoobi, Review of Nanoindentation Size Effect: Experiments and Atomistic Simulation, Crystals 7 (2017) 321.

[23] H. Bei, E.P. George, Microstructures and mechanical properties of a directionally solidified NiAl – Mo eutectic alloy, Acta Mater. 53 (2005) 69–77, https://doi.org/10.1016/j.actamat.2004.09.003.

[24] H. Bei, E.P. George, G.M. Pharr, Elastic constants of single crystal Cr3Si and Cr – Cr 3Si lamellar eutectic composites: A comparison of ultrasonic and nanoindentation measurements, Scr. Mater. 51 (2004) 875–879, https://doi.org/10.1016/j.scriptamat.2004.07.001.

[25] Y.Z. Xia, H. Bei, Y.F. Gao, D. Catoor, E.P. George, A Synthesis, characterization, and nanoindentation response of single crystal Fe – Cr – Ni alloys with FCC and BCC structures, Mater. Sci. Eng. A 611 (2014) 177–187, https://doi.org/10.1016/j.msea.2014.05.079.

[26] A. Ruiz-Moreno, P. Hähner, F. Fumagalli, V. Haiblikova, M. Conte, N. Randall, Stress−strain curves and derived mechanical parameters of P91 steel from spherical nanoindentation at a range of temperatures, Mater. Des. 194 (2020) 108950.

[27] P.S. Phani, W.C. Oliver, G.M. Pharr, An experimental assessment of methods for mitigating plasticity error during nanoindentation with continuous stiffness measurement, Mater. Des. 194 (2020) 108924.

[28] W. Chrominski, L. Ciupinski, P. Bazarnik, T. Markelj, T. Schwarz-Selinger, Microstructure evolution in helium implanted self-irradiated tungsten annealed at 1700 K studied by TEM, Mater. Charact. 174 (2021) 110991.

[29] A.P. Thompson, H.M. Aktulga, R. Berger, D.S. Bolintineanu, W.M. Brown, et al., LAMMPS - a flexible simulation tool for particle-based materials modeling at the atomic, meso, and continuum scales, Comp. Phys. Comm. 271 (2022) 108171.

[30] W. Choi, Y.H. Jo, S.S. Sohn, S. Lee, B. Lee, Understanding the physical metallurgy of the CoCrFeMnNi high-entropy alloy: an atomistic simulation study, Comput. Mater. 4 (2017) 1–9, https://doi.org/10.1038/s41524-017-0060-9.

[31] F.J. Domingues-Gutierrez, P.S. Krstić, Sputtering of lithiated and oxidated carbon surfaces by low-energy deuterium irradiation, J. Nucl. Mater. 492 (2017) 56–61, https://doi.org/10.1016/j.jnucmat.2017.05.014.

[32] F.J. Dominguez-Gutierrez, S. Papanikolaou, A. Esfandiarpour, P. Sobkowicz, M. Alava, Nanoindentation of single crystalline Mo: Atomistic defect nucleation and thermomechanical stability, Mater. Sci. Eng., A 826 (2021), https://doi.org/10.1016/j.msea.2021.141912 141912.

[33] L. Yen-Hung, J. Sheng-Rui, L. Yi-Shao, Y. Ping-Feng, Molecular Dynamics Simulation of nanoindentation-induced Mechanical Deformation and Phase Transformation in Monocrystalline Silicon, Nanoscale Res. Lett. (2008) 71–75, https://doi.org/10.1007/s11671-008-9119-3.

[34] I. Szlufarska, Atomistic simulations of nanoindentetion, Mater. Today 9 (5) (2006) 42–50, https://doi.org/10.1016/S1369-7021(06)71496-1.

[35] K. Jin, W. Guo, C. Lu, M.W. Ullah, Y. Zhang, W.J. Weber, J.D. Poplawsky, H. Bei, Effects of Fe concentration on the ion-irradiation induced defect evolution and hardening in Ni-Fe solid solution alloys, Acta Mater. 121 (2016) 365–373, https://doi.org/10.1016/j.actamat.2016.09.025.

[36] K. Jin, Y.F. Gao, H. Bei, Intrinsic properties and strengthening mechanism of monocrystalline Ni-containing ternary concentrated solid solutions, Mater. Sci. Eng. A 695 (April) (2017) 74–79, https://doi.org/10.1016/j.msea.2017.04.003.

[37] H. Song, H. Yavas, E. Van der Giessen, S. Papanikolaou, Discrete dislocation dynamics simulations of nanoindentation with pre-stress: Hardness and statistics of abrupt plastic events, J. Mech. Phys. Solids 123 (2019) 332–347.

[38] W.D. Nix, H. Gao, Indentation size effects in crystalline materials: a law for strain gradient plasticity, J. Mech. Phys. Solids 46 (1998) 411–425, https://doi.org/10.1016/S0022-5096(97)00086-0.

[39] Stukowski, Alexander. "Visualization and analysis of atomistic simulation data with OVITO–the Open Visualization Tool." Modelling and Simulation in Materials Science and Engineering 18, no. 1 (2009), 015012.

[40] W.J. Yang, R.A. Dodd, G.L. Kulcinski, Electron irradiation damage in high purity aluminium, J. Nucl. Mater. 64 (1977) 157–166, https://doi.org/10.1016/0022-3115(77)90019-8.

[41] K.G. Field, Y. Yang, T.R. Allen, J.T. Busby, Defect sink characteristics of specific grain boundary types in 304 stainless steels under high dose neutron environments, Acta Mater. 89 (2015) 438–449, https://doi.org/10.1016/j.actamat.2015.01.064.

[42] N. Hashimoto, J.D. Hunn, T.S. Byun, L.K. Mansur, Microstructural analysis of ion-irradiation-induced hardening in inconel 718, J. Nucl. Mater. 318 (2003) 300–306, https://doi.org/10.1016/S0022-3115(03)00013-8.

[43] S.I. Porollo, A.M. Dvoriashin, Y.V. Konobeev, F.A. Garner, Microstructure and swelling of neutron irradiated nickel and binary nickel alloys, J. Nucl. Mater. 442 (2013) S809–S812, https://doi.org/10.1016/j.jnucmat.2013.05.019.

[44] Y.N. Osetsky, D.J. Bacon, A. Serra, B.N. Singh, S.I. Golubov, Stability and mobility of defect clusters and dislocation loops in metals, J. Nucl. Mater. 276 (2000) 65–77, https://doi.org/10.1016/S0022-3115(99)00170-1.

[45] P. Xiu, H. Bei, Y. Zhang, L. Wang, K.G. Field, STEM characterization of dislocation loops in irradiated FCC alloys, J. Nucl. Mater. 544 (2021), https://doi.org/10.1016/j.jnucmat.2020.152658 152658.

[46] Y. Zhang, G.M. Stocks, K. Jin, Ch. Lu, H. Bei, B.C. Sales, L. Wang, L.K. Béland, R.E. Stoller, G.D. Samolyuk, M. Caro, A. Caro, W.J. Weber, Influence of chemical disorder on energy dissipation and defect evolution in nickel and Ni-based concentrated solid solution alloys, Nat. Commun. 6 (2015) 8736.

[47] S. Zhao, Y. Osetsky, Y. Zhang, Preferential diffusion in solid solution alloys: NiFe NiCo and NiCoCr, Acta Materialia 128 (2017) 391.

[48] K. Jin, W. Guo, Ch. Lu, M.W. Ullah, Y. Zhang, W.J. Weber, L. Wang, J.D. Poplawsky, Hongbin Bei, Effects of Fe concentration on the ion-irradiation induced defect evolution and hardening in Ni-Fe solid solution alloys, Acta Mater. 121 (2016) 365.

[49] Y. Zhang, K. Jin, H. Hue, Ch. Lu, R.J. Olsen, L.K. Beland, M.W. Ullah, S. Zhao, H. Bei, D.S. Aidhy, G.D. Samolyuk, L. Wang, M. Caro, A. Caro, G.M. Stocks, B.C. Larson, I.M. Robertson, A.A. Correa, W.J. Weber, Influence of chemical disorder on energy dissipation and defect evolution in advanced alloys, J. Mater. Res. 31 (2016) 2363.

[50] C. Lu, K. Jin, L.K. Béland, F. Zhang, T. Yang, L. Qiao, Y. Zhang, H. Bei, H.M. Christen, R.E. Stoller, L. Wang, Direct observation of defect range and evolution in ion-irradiated single crystalline Ni and Ni binary alloys, Sci. Rep. 6 (2016) 19994.

[51] S. Zhao, Y. Osetsky, G.M. Stocks, Y. Zhang, Local-environment dependence of stacking fault energies in concentrated solid-solution alloys, npj Comput. Mater. 5 (2019) 13.

[52] S. Zhao, Y. Osetsky, G.M. Stocks, et al., Local-environment dependence of stacking fault energies in concentrates solid-solution alloys, NPJ Comp. Mater. 5 (2019) 13.

[53] X.-X. Wang, L.-L. Niu, S. Wang, Energetics analysis of interstitial loops in single-phase concentrated solid-solution alloys, J. Nucl. Mater. 501 (2018) 94–103.

[54] S. Zhao, Y. Osetsky, Y. Zhang, Diffusion of point defects in ordered and disordered NieFe alloys, J. Alloys Comp. 805 (2019) 1175.

[55] B. Sadigh, P. Erhart, A. Stukowski, et al., Scalable parallel Monte Carlo algorithm for atomistic simulations of precipitation in alloys, Phys. Rev. B 85 (2012) 184203.

[56] Q.-J. Li, H. Sheng, E. Ma, Strengthening in multi-principal element alloys with local-chemical-order roughened dislocation pathways, Nat. Commun. 10 (2019) 1.

[57] A.J. Zaddach, C. Niu, C.C. Koch, D.L. Irving, Mechanical properties and stacking fault energies of NiFeCrCoMn high-entropy alloy, J. Met. 65 (2013) 1780.

[58] S. Zhao, Y. Osetsky, Y. Zhang, Preferential diffusion in concentrated solid solution alloys: NiFe, NiCo, and NiCoCr, Acta Mater. 128 (2017) 391–399.